Hindawi
Advances in Materials Science and Engineering
Volume 2018, Article ID 8267631, 15 pages
https://doi.org/10.1155/2018/8267631

Research Article

Activated Hydrotalcites Obtained by Coprecipitation as Photocatalysts for the Degradation of 2,4,6-Trichlorophenol

Esthela Ramos-Ramírez,[1] **Norma Gutiérrez-Ortega**,[2] **Francisco Tzompantzi**,[3] **Claudia M. Gómez**,[1] **Gloria del Angel**,[3] **Gabriel Herrera-Pérez**,[4] **Alma Hortensia Serafín-Muñoz**,[2] **and Clara Tzompantzi-Flores**[3]

[1]*Departamento de Química, División de Ciencias Naturales y Exactas, Universidad de Guanajuato, Noria Alta s/n, Col. Noria Alta, 36050 Guanajuato, GTO, Mexico*
[2]*Departamento de Ingeniería Civil, División de Ingenierías, Universidad de Guanajuato, Juárez No. 77, Col. Centro, 36000 Guanajuato, GTO, Mexico*
[3]*Universidad Autónoma Metropolitana - Iztapalapa, Depto. Química, Ecocatal, Av. San Rafael Atlixco No. 186, 09340 Ciudad de México, Mexico*
[4]*Instituto Tecnológico Superior de Irapuato, Carretera Irapuato - Silao km 12.5 Colonia El Copal, 36821 Irapuato, GTO, Mexico*

Correspondence should be addressed to Esthela Ramos-Ramírez; ramosre@ugto.mx and Norma Gutiérrez-Ortega; normagut@ugto.mx

Received 28 June 2018; Revised 4 October 2018; Accepted 31 October 2018; Published 2 December 2018

Academic Editor: Frederic Dumur

Copyright © 2018 Esthela Ramos-Ramírez et al. This is an open access article distributed under the Creative Commons Attribution License, which permits unrestricted use, distribution, and reproduction in any medium, provided the original work is properly cited.

A gallery of hydrotalcite-type mesoporous materials with different Mg/Al molar ratios were synthesized by the coprecipitation method. The materials were activated by heat treatment to test their activity in the photodegradation of 2,4,6-trichlorophenol under UV light irradiation. The physicochemical properties of the different synthesized and activated materials were determined using XRD, physical adsorption/desorption of N_2, FTIR, SEM, DTA, and TGA. Their banned band energy was determined by UV-Vis to identify their potential to be used as a semiconductor in catalytic photodegradation processes. The results of photodegradation tests of 2,4,6-trichlorophenol showed that hydrotalcites have a high degradation capacity, up to 100% for the catalyst of Mg/Al ratio = 2, with a high mineralization capacity of 80%. The degradation capacity of most of the catalysts tested is mainly due to the presence of holes and the formation of superoxide free radicals, which are the determining species within the degradation mechanism.

1. Introduction

Due to the worldwide increase in the quantity and variety of chemical products used both for domestic use and for industrial use, the presence of emerging pollutants has increased [1, 2]. Currently, more than two thousand species of emerging pollutants have been identified in surface water reservoirs. Among the main emerging polluters are pharmaceutical products, cosmetics, surfactants, additives, and pesticides, among others [3–5]. Chlorophenols are a group of chemicals that are formed by adding chlorines (between one and five) to phenol. There are five basic types of chlorophenols: monochlorophenols, dichlorophenols, trichlorophenols, tetrachlorophenols, and pentachlorophenols. In total, there are 19 different chlorophenols. Chlorophenol and its derivatives are widely used as intermediates in the manufacture of pharmaceuticals, synthetic dyes, petrochemicals, biocides, pesticides, insecticides, textiles, leather treatment products, and wood preservatives [6–8]. Chlorophenols are deposited in the environment mainly through the direct discharge of industrial waste [9–11]. By estimation, the annual production of chlorophenols is approximately 200,000 tons, and in the US alone, there are about 2,000 tons of chlorophenol compounds wastes in industries dedicated to the production of insecticides, paper, and wood and in petroleum refineries [12–14]. Chlorophenols are considered refractory pollutants that when poured into ecosystems can cause serious problems to the environment and to the species

that inhabit it, including humans. Adverse effects on human health range from irritation of the skin and respiratory tract to convulsions, wheezing, endocrine system damage, coma, and death. US Environmental Protection Agency (USEPA) places them within the list of priority pollutants and has determined that 2,4,6-trichlorophenol is a probable carcinogen [15–17].

The technologies that have been implemented for the elimination of phenolic contaminants present in water are classified mainly into two large groups: those that separate the contaminant, such as adsorption, extraction, distillation, and ultrafiltration with membranes, and those that degrade the contaminant, for example, supercritical oxidation, moist air treatment, thermal treatment, biodegradation, and catalytic degradation [18–25]. In recent years, the processes of advanced oxidation using photocatalysts have generated great expectations as effective and effective methods for the elimination of emerging contaminants. The materials that are used mainly for these processes are metallic semiconductors such as TiO_2, ZnO, SnO_2, ZrO_2, V_2O_5, WO_3, and CeO_2, among others; there is a great variety and quantity of investigations on them [26–31]. Specifically, titanium dioxide (TiO_2) is the most widely used and studied photocatalyst because it has a high stability in its chemical structure, is nontoxic, and is relatively inexpensive. However, TiO_2 has some disadvantages, such as the relatively high value of banded band energy (approximately 3.2 eV for anatase and 3.0 eV for rutile), which limits its absorption in the spectrum of the UV-Vis region, besides presenting a high rate of recombination of electrons and photoinduced holes that decreases their photocatalytic activity. Therefore, to reduce band gap energy, several studies have focused on the doping of TiO_2 with metal ions such as nickel, manganese, cobalt, titanium, chromium, iron, vanadium, zinc, and copper, among others, as well as with nonmetallic elements such as nitrogen, carbon, and fluorine, or even through the formation of composites with MnO_2, In_2O_3, CeO_2, and MoS_2 [32–43].

An alternative that is taking relevance is the application of materials that are not considered as semiconductors but that are nevertheless demonstrating the ability to photodegrade emerging substances such as dyes and medicines. Such is the case of materials such as alumina, zeolites, and some simple and mixed metal oxides, among others. Within this group of materials, hydrotalcites have increased their relevance in recent years to be used as photocatalysts for the degradation of organic compounds. The hydrotalcites that have been studied the most are those that contain Mg, Zn, and Al in their structure, which have demonstrated a high degradation capacity for azo-like dyes, but for the degradation of persistent organic compounds, it has been necessary to resort to use of doping agents to improve. Hydrotalcites are materials of the anionic clays type consisting of sheets of mixed metal hydroxides that generate a positive charge in the sheets and that are neutralized by anions that are in the interlaminar spaces. The method of synthesis of hydrotalcites as well as the conditions of thermal treatment of hydrotalcites to thermally evolve them to mixed metal oxides can influence the formation of metal oxide nanoparticles with porous structures, larger and better reactive sites, and superparamagnetic properties [44–46]. This article describes the synthesis conditions of hydrotalcites and the effect of the metallic Mg/Al ratio in obtaining activated hydrotalcites to improve the photocatalytic properties of hydrotalcites in the degradation of 2,4,6-trichlorophenol without need to dope with some transition metals.

2. Experimental

2.1. Obtaining Photocatalysts

2.1.1. Synthesis of Mg/Al-Type Hydrotalcite Catalytic Precursors of Ratios 1, 2, 3, 4, 5, 6, and 7. They were synthesized by the coprecipitation method. The Mg/Al hydrotalcite of ratio 1 was obtained by coprecipitating a solution with 1 mol of magnesium nitrate hexahydrate and 1 mol of aluminum nitrate nonahydrate, with a basic solution of sodium hydroxide. The coprecipitation was carried out at a pH of 11.5. The coprecipitate was refluxed for 2 hours with a subsequent aging for 24 hours. The precipitated solid was washed to a pH of 9 and then dried at 100°C. The hydrotalcites of relation 2, 3, 4, 5, 6, and 7 were obtained with the same methodology, but varying the molar amount of each of the magnesium and aluminum sources to obtain the desired molar ratio. The materials were identified as M1, M2, M3, M4, M5, M6, and M7 that correspond to those that represent Mg/Al ratio, respectively.

2.1.2. Activation of Hydrotalcites. The synthesized hydrotalcites were thermally treated at 500°C in air atmosphere for 4 hours for the formation of the mixed Mg/Al oxides and were identified as M1 500°C, M2 500°C, M3 500°C, M4 500°C, M5 500°C, M6 500°C, and M7 500°C.

2.2. Structural Characterization of Catalytic Precursors and Catalysts. The thermal evolution profiles, differential thermal analysis (DTA), and thermogravimetric analysis (TGA) were determined in the TA Instruments Thermo Analyzer (at a heating rate of 10°C/min in air atmosphere at a speed of 100 mL/min and using α-alumina as the reference standard). The textural properties of the solids, such as the surface area using Brunauer–Emmett–Teller (BET) theory, pore size, and pore diameter, were determined by physisorption of N_2 at −196°C in a Micromeritics ASAP 2010 Analyzer. The pore size distribution was calculated from the desorption curves of the Barrett–Joyner–Halenda (BJH) isotherms. The crystalline phases of the samples synthesized and thermally treated at 400°C were analyzed by X-ray diffraction (XRD) using an INEL Equinox Powder Diffractometer (copper anode, monochromatic CuKα radiation with a wavelength (λ) of 1.5418 Å). The surface hydroxyl groups analyzed with an infrared spectroscope (das de Fourier (FTIR) Perkin Elmer 1600) would be in a region with a wavenumber of 1000 to 4000 cm^{-1}. To verify the optimal working range of the solids as photocatalysts, the UV-Vis spectra by diffuse reflectance spectroscopy (DRS) were determined in a Perkin Elmer Lambda UV-Vis-NIR spectrophotometer. The band gap energy (E_g) of the samples was calculated from the ultraviolet absorption spectra of diffuse reflectance, considering that

E_g = (1239b/−α), where α and b are coefficients that were linearized in the region-appropriate spectrum.

2.3. Photocatalytic Activity Tests on the Degradation of 2,4,6-Trichlorophenol. The photocatalytic degradation capacity of 2,4,6-trichlorophenol using the materials obtained was determined under the following conditions: standard solution of 100 ppm of 2,4,6-trichlorophenol was placed in a batch reactor at a controlled temperature of 25°C with constant magnetic stirring of 700 rpm, a flow of air of 1 mL/s, a UV light irradiation of 254 nm, and an emission of 2.5 mW/cm^2 generated by a Pen-Ray UV lamp inserted in a quartz tube. A dilute aqueous solution (100 mg/L) of 2,4,6-trichlorophenol was prepared; 200 mL of the solution and 200 mg of the photocatalyst to be analyzed were poured into a batch reactor, and TiO_2-P25 was used as a reference material. Prior to UV irradiation, the catalyst was contacted with the standard solution of 2,4,6-trichlorophenol for a period of 1 hour in the dark to verify an adsorption-desorption equilibrium of the contaminating molecule with the catalyst. Once equilibrium was reached, irradiation was started for 2 hours. Additionally, a sample of 2,4,6-trichlorophenol solution was subjected to photolysis in the absence of a catalyst to determine the effect of the radiation on the contaminant. In addition, for the comparison against a reference photocatalyst, commercial TiO_2-P25 was used. In all cases, the pollutant degradation process was monitored by means of sampling of reactor aliquots, with the subsequent quantification of this in a UV-Vis Cary 100 spectrophotometer at a wavelength of 310.5 nm. The amount of total organic carbon present in the irradiated solution was determined in a Shimadzu TOC 5000.

2.4. Detection of Hydroxyl and Superoxide Radicals and Study of Hole Trap. The quantification of the $OH^{\bullet}$ radicals generated by the photocatalyst during photocatalytic degradation was determined by the formation of 7-hydroxycoumarin, which was followed by a Fluorescence Spectroscopy Scinco FS-2 spectrometer. A dilute aqueous solution (2×10^{-3} M) of coumarin was prepared; 200 mL of the solution and 200 mg of the photocatalyst to be analyzed were poured into a batch reactor, and TiO_2-P25 was used as a reference material. In the same way, the study was carried out in the absence of photocatalyst (photolysis) to observe the possible production of hydroxyl radicals. Once the above study was done, the solution was irradiated with UV light for 1 hour with a Pen-Ray lamp (λ = 254 nm and I0 = 4.4 mWcm^{-2}), with the conditions of constant stirring, oxygen bubbling, and temperature (800 rpm, 1 mL/s, and 25°C, respectively), extracting 3 mL aliquots at five-minute intervals. Finally, the fluorescence emission spectra in the irradiated solution were analyzed by photoluminescence, at a wavelength of 320 nm. In addition, the determination of the influence of the absence of bubbled oxygen and therefore absence of superoxide radicals (bubbled reaction with nitrogen) was carried out. In this test, 200 mg of the photocatalyst and 200 mL of the 2,4,6-trichlorophenol solution at 100 ppm with a nitrogen flow of 1 mL/s were used. The reaction was carried out for 2 hours, extracting aliquots in a 15 min interval.

3. Results and Discussion

3.1. Effect of Thermal Treatment on the Physicochemical Properties of Hydrotalcites with Different Mg/Al Molar Ratios

3.1.1. Structural Analysis of the Synthesized Hydrotalcites. In Figure 1, X-ray diffractograms of the materials obtained by coprecipitation are shown. As it is possible, all the materials synthesized independently of the Mg/Al relation present the crystalline structure identified as hydrotalcite when observing the characteristic signals (003), (006), (009), (015), (018), (110), and (113) (JCPDS card 22-0700). As noted, there is a slight shift to the left of the signals as the Mg/Al ratio increases. This is directly related to the amount of aluminum present in the crystal lattice, such that as the amount of aluminum decreases, the peaks are offset to a higher value of 2θ, which is associated with a lower positive interlaminar load and as a consequence to a smaller quantity of anions lodged in the interlaminar space. Another property that is modified with the variation of the Mg/Al ratio is the crystallinity. As the amount of aluminum in the network increases, the crystalline peaks become more sharp and intense which is interpreted as a greater crystalline perfection. In the case of solid M1, it can be observed that a small crystalline phase of aluminum was secreted because it is in excess with respect to the amount of magnesium, where the excess was not incorporated into the brucite network (Mg $(OH)_2$).

The main characteristic peaks of the hydrotalcites are (003) and (110), which appear approximately in 11 and 60° of 2θ, which provide information of the basal spacing d (003) and the intercationic distance "a," respectively. From them, it is possible to calculate the cell parameters "c" and "a" (Table 1), using Bragg's law and assuming a hexagonal stacking. The parameter "c" = 3 × d (003) corresponds to the spacing of three sheets with their respective interlaminar regions, while the parameter "a" = 2 × d (110) indicates the average cation-cation distance. The value of the cation-cation distance showed that when increasing the Mg/Al molar ratio, there is no significant change in the parameter a ("a" = 3.07 ± 0.03 Å), which is similar to that obtained from a commercial hydrotalcite (Aldrich); however, for parameter c, a change is observed, which indicates that in the direction of the plane (hk0), the cell is modified, with values being reported in the range from 22.30 to 25.93 Å. As can be seen, another important parameter is the basal spacing d (003), which is equal to the sum of the thickness of a layer of the hydrotalcite (~4.8 Å) and the interlaminar distance (~3.0 Å) [47] where the interlaminar distance is related to the size of the anions, the degree of hydration, and the quantity of anions in the intermediate layer [48]. The distance of layer d (003) also decreased with the increase in the ratio of the values of d (003) which indicates a variation in the quantity of CO_3^{2-} ions (interlaminar anions of charge compensation) and intercalated water molecules [49].

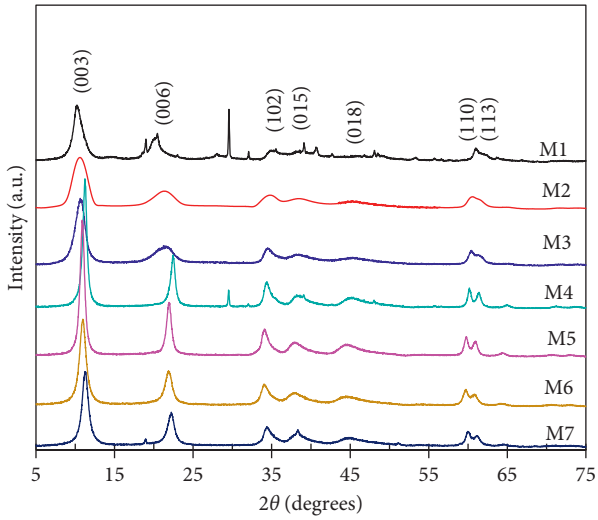

Figure 1: X ray diffraction of fresh Mg/Al hydrotalcites with different Mg/Al ratios.

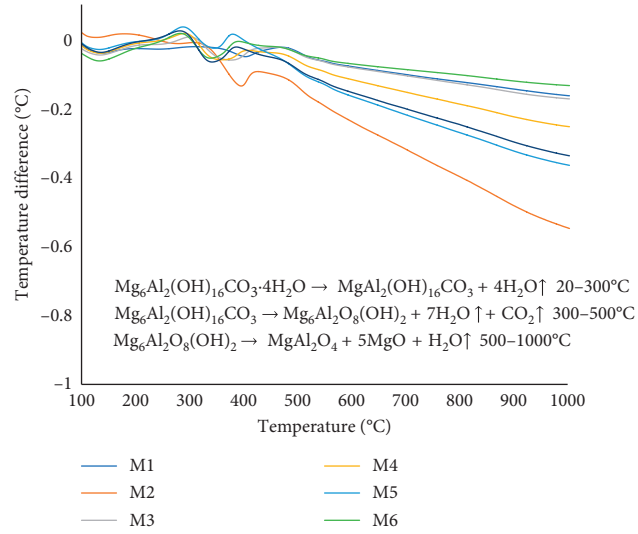

Figure 2: Differential thermal analysis of Mg/Al hydrotalcites with different Mg/Al ratios.

Table 1: Network parameters of hydrotalcite-type photocatalysts M1 to M7.

Photocatalyst	d (003)	Parameter "c" (Å)	Parameter "a" (Å)	Interlamellar d (Å)
M1	8.64	25.93	3.03	3.84
M2	8.16	24.50	3.00	3.37
M3	8.32	24.95	3.06	3.52
M4	7.87	23.60	3.07	3.07
M5	8.12	24.38	3.09	3.31
M6	8.06	24.17	3.10	3.26
M7	7.88	23.65	3.08	3.08
M (Aldrich)	7.63	22.90	3.05	2.84

3.1.2. Thermal Evolution Profile of the Hydrotalcites Synthesized. In Figure 2, DTA of the hydrotalcites M1 to M7 is shown. In all cases, it observes an endothermic reaction centered at 143°C, due to the elimination of molecules occluded in the crystalline structure, followed by endothermic reactions at 302°C to 425°C. For the case of solids M7 to M4, the evolution to periclase (MgO) and spinel ($MgAl_2O_4$) occurs at lower temperatures below 400°C. In the case of solid M2, the same profile of thermal decomposition is observed; however, a greater stability up to 500°C is observed, which is attributed to the greater crystallinity that it presents, which favors the activation of the catalyst. The thermal decomposition reactions of the hydrotalcites associated with the endothermic reactions are shown directly in the figure.

In the TGA curves of Figure 3, we can observe the seven hydrotalcites have a very similar thermogravimetric profile, although with more pronounced inflections as the Mg/Al ratio increases because the evolution of the phases is favored by having a greater amount of magnesium. The first loss is between 5 and 7.5% up to 200°C, which is attributed to the desorption of water absorbed in the material. The second weight loss is due to a loss ranging from 25 to 31% centered between 2500 and 400°C

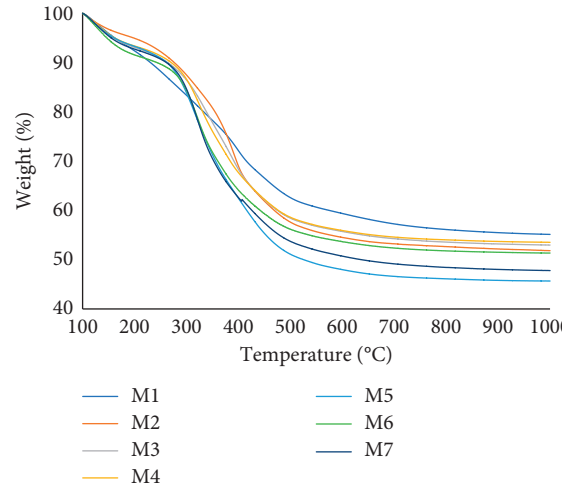

Figure 3: Thermogravimetric analysis of Mg/Al hydrotalcites.

which is attributed to the decomposition of bound hydroxyl groups and the elimination of interlaminar carbonate ions. The solids show a thermal stability between 400 and 500°C with a total mass loss of 49 to 54.3% based on the increase in the molar ratio, respectively. After 500°C, the lamellar structure finally collapses to segregate the amorphous phase of the mixed oxide Mg/Al and the crystalline phase of periclase, which can be identified by an XRD analysis of the solids at 500°C. The stability up to this temperature allows the reconstruction by the memory effect and potentially the photocatalytic activity as a function of the Mg/Al ratio.

With the study of the thermal behavior of the obtained hydrotalcites, the optimum activation temperature was found, which corresponds to 500°C, to guarantee that the solid is in the catalytically active phase for the photodegradation process in the form of metallic oxides.

3.1.3. Structural and Textural Properties of Mixed Oxides Obtained by Thermal Evolution When Activating Hydrotalcites at 500°C before Photodegradation. Figure 4 shows the X-ray diffraction pattern of hydrotalcites calcined at 500°C. It can be observed that the solids M7 to M3 treated at 500°C show the presence of the crystalline phase of periclase (MgO) (JCPDS- 4-0829), increasing the crystallinity when increasing the Mg/Al ratio. In the case of solid M2, it is observed that it has also evolved at 500°C but has a lower crystallinity because at that temperature there has only been the phase change. Only in the case of solid M1, there is a crystalline-phase mixture due to the crystalline phase secreted from excess aluminum. According to the thermal analysis, in addition to the crystalline phase of periclase, an amorphous phase of spinel ($MgAl_2O_4$) is present.

Figure 5 shows the FTIR spectra of the hydrotalcites activated at 500°C before the photodegradation in which it is observed that there are no signals in the range of 4000 to 3000 cm^{-1} corresponding to the hydroxyl groups because the phases have evolved to amorphous and periclase spinel as confirmed by XRD. A signal is observed at 1460 cm^{-1}, corresponding to carbonate groups with different percentages of transmittance in the following order: M1 > M4 > M7 > M6 > M2 > M5 > M3, due to thermal activation.

In Figure 6, N_2 adsorption-desorption isotherms of hydrotalcites activated at 500°C before photoreaction are shown. As can be seen, in all cases, the isotherms are of type IV with hysteresis cycles of type H2, associated with capillary condensation produced in the mesopores of materials in the form of sheets or plates, where the pores are large with a small opening.

Table 2 shows the values of the specific areas determined by the BET method of hydrotalcites activated at 500°C and the average pore size calculated by the BJH method. As it is observed, the specific area decreases as the Mg/Al ratio increases, with the M2 catalyst being the one with the highest specific area of 95.21 m^2/g and M7 with the lowest value of 2.36 m^2/g.

For the case of the M6 and M7 solids, the decrease of the specific area is attributed to the thermal evolution by the thermal treatment at 500°C, which causes the structure of the hydrotalcite to collapse for the formation of the spinel and periclase phases. For the case of solids M1 to M5, the decrease in porosity is associated with the lower amount of aluminum in the sheets, which generates a lower accumulation of carbonates and molecules in the interlayer, so when the photocatalyst is activated, a lower porosity is generated in the solid.

Figure 7 shows the scanning microphotograph of activated hydrotalcites M2 and M3, in which crystals of heterogeneous size with numerous edges are observed and in which the laminar structure of the solid can be seen. The activated hydrotalcite M2 shows a higher crystallinity and smaller particle size than M3, which favors the catalytic capacity.

3.2. UV-Vis Reflectance Diffuse Spectroscopy. Figure 8 shows the UV-Vis spectrum of diffuse reflectance, where the

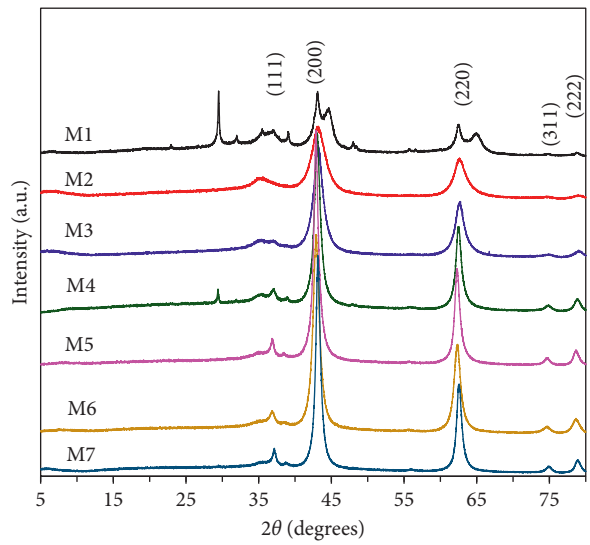

Figure 4: X ray diffraction of Mg/Al hydrotalcites with different Mg/Al ratios activated at 500°C before photoreaction.

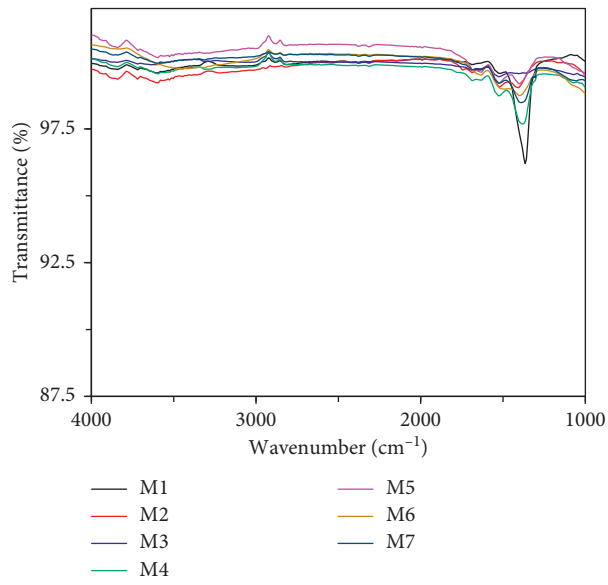

Figure 5: Infrared spectra of the photocatalysts Mg/Al-activated hydrotalcites at 500°C before photocatalytic degradation of 2,4,6-trichlorophenol.

values of band gap energy (E_g) are observed for catalysts activated at 500°C before photodegradation at a wavelength of maximum absorption at λ = 265 nm. Hydrotalcites activated at 500°C have an E_g value ranging from 2.86 to 3.29 eV (Table 3).

As can be seen, the catalysts present banned band energy values between 3.45 and 3.56 which are early than the E_g value of positive control for photocatalytic degradation, TiO_2 [50]. According to these values of E_g for the solids, they are postulated as photocatalysts with potential for their application in the degradation with greater efficiency; however, also the other photocatalysts that are very close to TiO_2 could have a good degradation capacity.

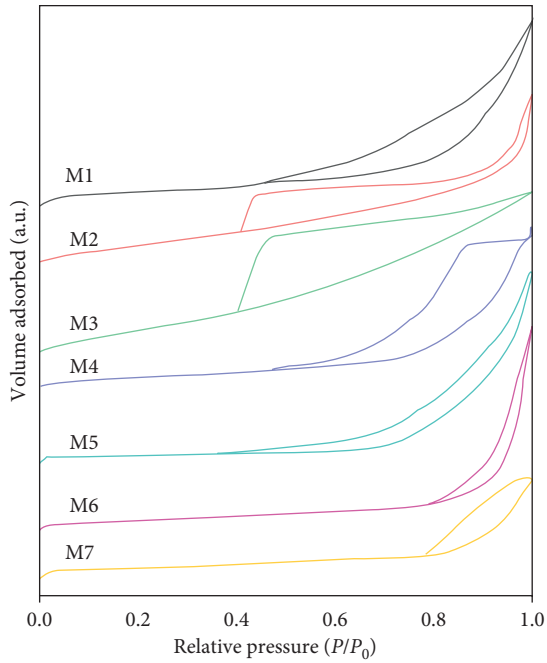

Figure 6: N_2 adsorption-desorption isotherms of activated hydrotalcites before photodegradation.

Table 2: Textural properties of activated hydrotalcites.

Photocatalyst	Surface area (m^2/g)	Pore volume (cm^3/g)	Pore size (nm)
M1 500°C	92.35	0.3706	16.0
M2 500°C	95.21	0.1719	7.2
M3 500°C	70.07	0.1158	6.2
M4 500°C	52.48	0.2739	20.9
M5 500°C	23.00	0.3554	61.8
M6 500°C	7.43	0.1044	56.2
M7 500°C	2.36	0.0468	79.5

3.3. Photocatalytic Degradation of 2,4,6-Trichlorophenol. In Figure 9, the UV-Vis spectra are shown during the photocatalytic reaction for the degradation of 2,4,6-trichlorophenol, and the reaction system was followed for 240 minutes for each of the hydrotalcites activated at 500°C, as well as TiO_2-P25 as a positive control. For all materials, no variations were observed in the adsorption spectra of the molecule during the first hour of adsorption (absence of light), which indicates that the molecule was not adsorbed by the catalyst. In these spectra, the absorption drop in the wavelength at $\lambda = 310.5$ nm is observed from the ignition of the irradiation source, which is characteristic for the 2,4,6-trichlorophenol molecule, and this indicates the degradation of the corresponding contaminant, including the aromatic part.

As can be seen for the case of the M1 and M4 catalysts, the band at time zero was centered at 310 nm, and as the irradiation time passes, it suffers a phase shift towards 285 nm, which can be associated with the degradation of 2,4,6-trichlorophenol to 2,4-trichlorophenol. With respect to the overlapping double band centered at 210 and 225 nm at the initial time, it can be seen that the signal at 225 nm decreases as time passes until only the signal is visible at 210 nm; the said modification of the signal is associated with the primary band of the phenol resulting from the elimination of the chlorine atoms, and the catalysts M1 and M4 require more than 240 min for degradation. On the contrary, the rest of the catalysts, including TiO_2, do not show phase shift of the band centered at 310 nm at time zero, but only a decrease in this signal intensity can be observed, associated with the rapid degradation of the molecule 2,4,6-trichlorophenol. For the case of the band centered at 225 nm, it can be seen that in TiO_2, there is also a fade of the 225 nm band, the band being more visible at 210 nm due to the formation of phenol; while for the catalysts M2, M3, M5, M6, and M7, the definition of the band at 210 nm is accompanied by a significant decrease in intensity, which is associated with the fast degradation of the aromatic ring; it is faster for the case of the M2 catalyst which at 240 min has practically degraded [51]. According to the obtained results, it was observed that samples M2, M3, and M6 present better photocatalytic activity. The most active catalyst was M2 500°C since the degradation takes place more quickly during the first 90 minutes, followed by M6 and M3. The rest of the catalysts perform the degradation process a little more slowly and gradually, requiring up to 150 minutes to achieve greater degradation for the case of M4, M5, and M7 and up to 180 minutes for the case of M1. At the maximum contact time, 240 minutes of degradation, TiO_2 has a lower photodegradation capacity, compared to hydrotalcites activated at 500°C; whereas at 180 minutes, only one-third has degraded.

In Figure 10, the rate of degradation of 2,4,6-trichlorophenol is shown as a ratio of the number of molecules degraded per unit of time. The highest degradation capacity was presented by the M2 catalyst, which reached values of degradation of 2,4,6-trichlorophenol of 100%, and it is followed by the M3 catalyst with 98.8%, M6 with 98.7%, and so on, decreasing this capacity for solids M5, M7, M4, and M1 up to values of 84%, where the decrease in the degradation capacity is associated with the physicochemical properties of the materials obtained by coprecipitation such as the crystallinity and the thermal stability [52].

3.4. Detection of Hydroxyl and Superoxide Radicals and Study of Hole Trap. To propose the mechanism of photocatalytic degradation, the samples with the most photocatalytic activity were selected to perform the following tests: (1) observation of possible production of hydroxyl radicals, (2) influence of the absence of bubbled oxygen and therefore absence of superoxide radicals (bubbled reaction with nitrogen), and (3) influence of the gaps in the photocatalytic process by means of ammonium oxalate as a hole collector.

The possible formation of $OH^{\bullet}$ radicals by fluorescence spectroscopy was analyzed. For the detection of the said radicals, coumarin was used as a molecule that captures the radicals, producing 7-hydroxycoumarin. The reactions were carried out for one hour to avoid degradation of 200 mL of a

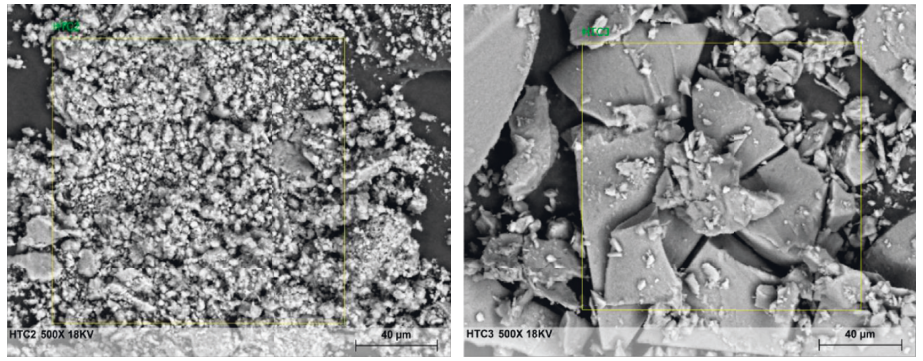

(a) (b)

Figure 7: SEM micrograph of activated hydrotalcites M2 (a) and M3 (b) at 500x and at 1200x.

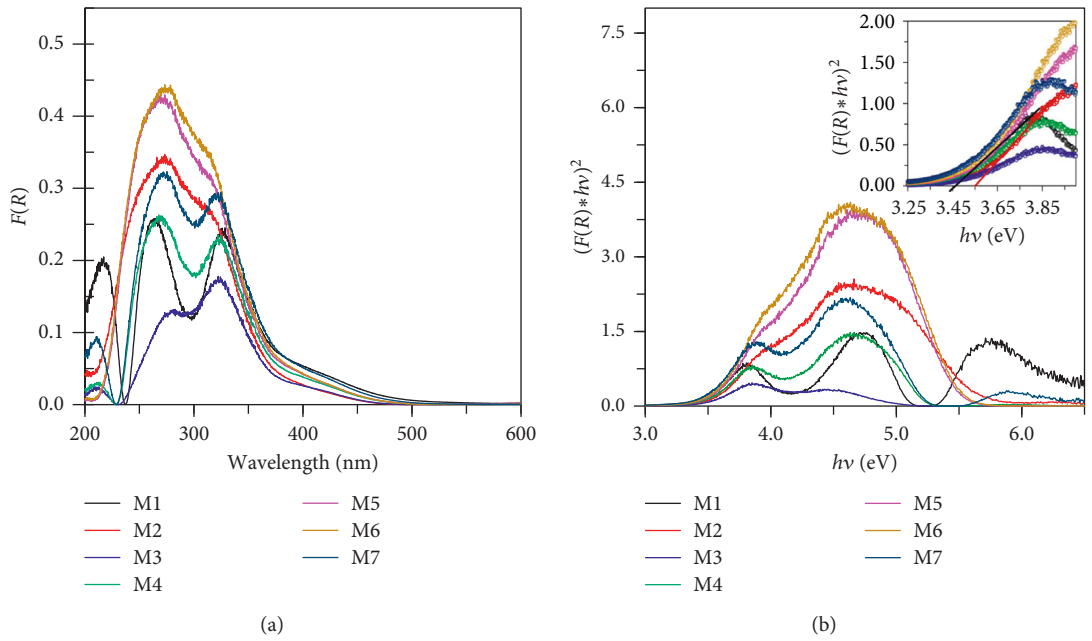

(a) (b)

Figure 8: (a) UV-Vis reflectance diffuse spectra of activated hydrotalcites at 500°C with different Mg/Al molar ratios before photoreaction. (b) Kubelka–Munk transformed diffuse reflectance spectra.

Table 3: Banned band energy of activated hydrotalcites determined from the Tauc plot.

Photocatalyst	Banned band (eV)
M1 500°C	3.45
M2 500°C	3.54
M3 500°C	3.47
M4 500°C	3.47
M5 500°C	3.51
M6 500°C	3.56
M7 500°C	3.48
Degussa TiO_2	3.20

2×10^{-3} M solution of coumarin with 20 mg of the catalyst, extracting 3 mL aliquots for 10 minutes. The selected samples were M2, M3, and M6, as seen in Figure 11 [53].

According to the results obtained, as seen in Figure 11, for the photolysis and the catalysts M2, M3 and M6 there is a lower intensity of the detection signal of the hydroxyl radicals, in comparison with the TiO_2-P25. In the case of photocatalysts M3 and M2, the production of hydroxyl radicals is quite close to that obtained by photolysis so that in these catalysts, there is no production of hydroxyl radicals. In the case of photocatalyst M6, greater intensity is observed compared with photolysis; however, this intensity is still lower than that obtained with TiO_2-P25. So, it is concluded that the hydroxyl radicals are not determinant using these catalysts. To determine the influence of the absence of bubbled oxygen and therefore absence of superoxide radicals (bubbled reaction with nitrogen), photocatalyst M2 was used because it has the best photocatalytic activity with a solution of 100 ppm of 2,4,6-trichlorophenol in N_2 atmosphere. The results are shown in Figure 12, from which it is observed that the photocatalytic activity decreases with the presence of ammonium oxalate, which is why the holes are determinant species in the photocatalytic mechanism, as well as the superoxide radicals.

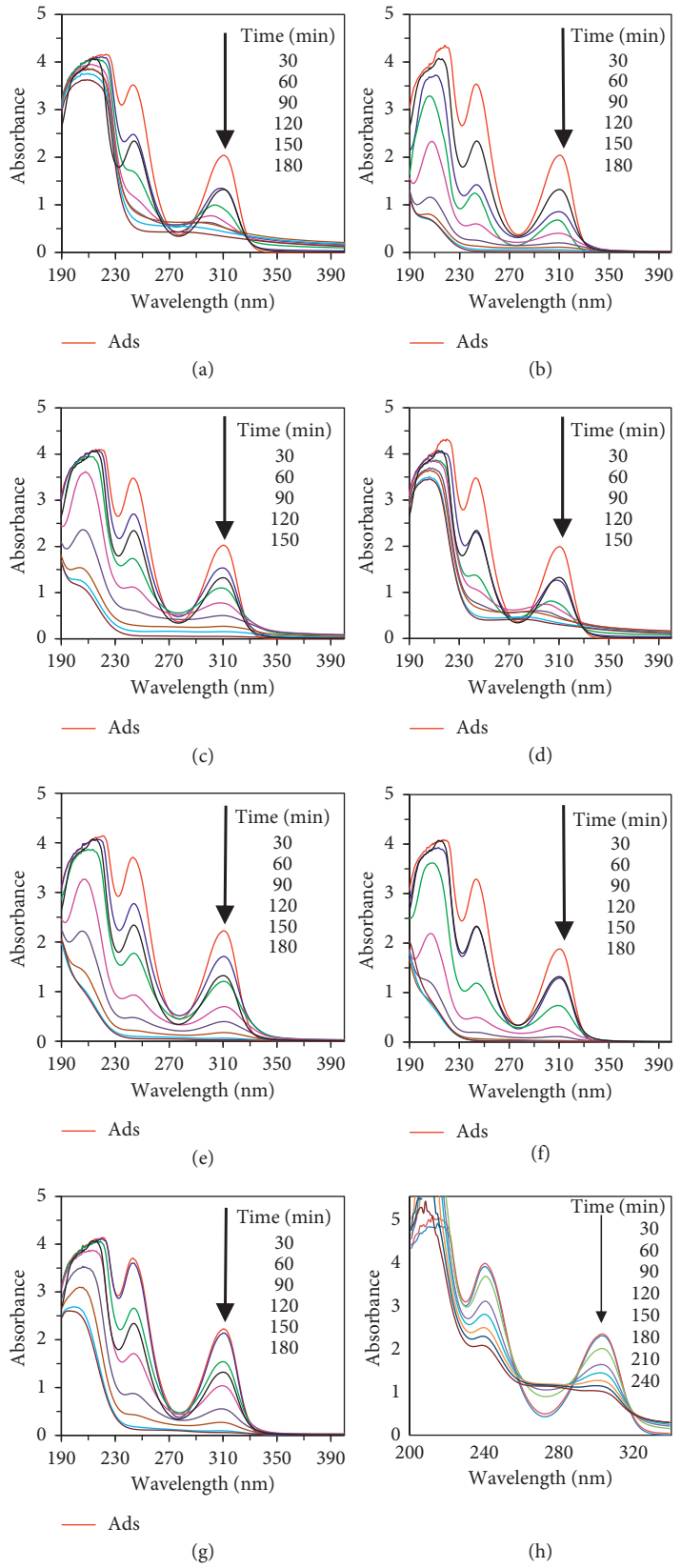

FIGURE 9: Absorption spectra of 100 ppm of 2,4,6-trichlorophenol in the presence of different photocatalysts under UV light irradiation over time. (a) M1. (b) M2. (c) M3. (d) M4. (e) M5. (f) M6. (g) M7. (h) TiO_2-P25.

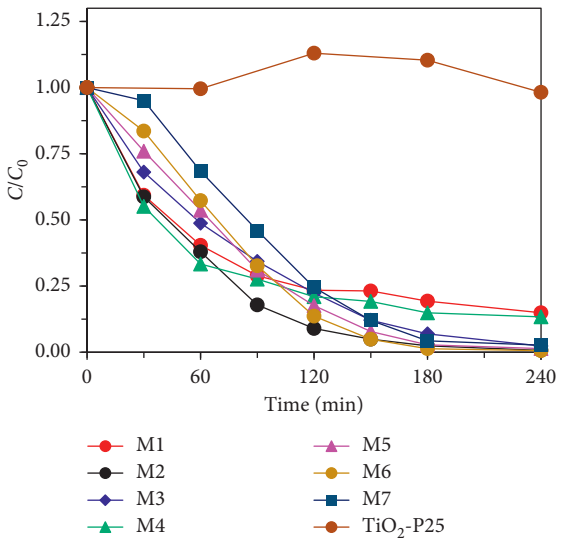

Figure 10: Relative degradation rate of 100 ppm of 2,4,6-trichlorophenol.

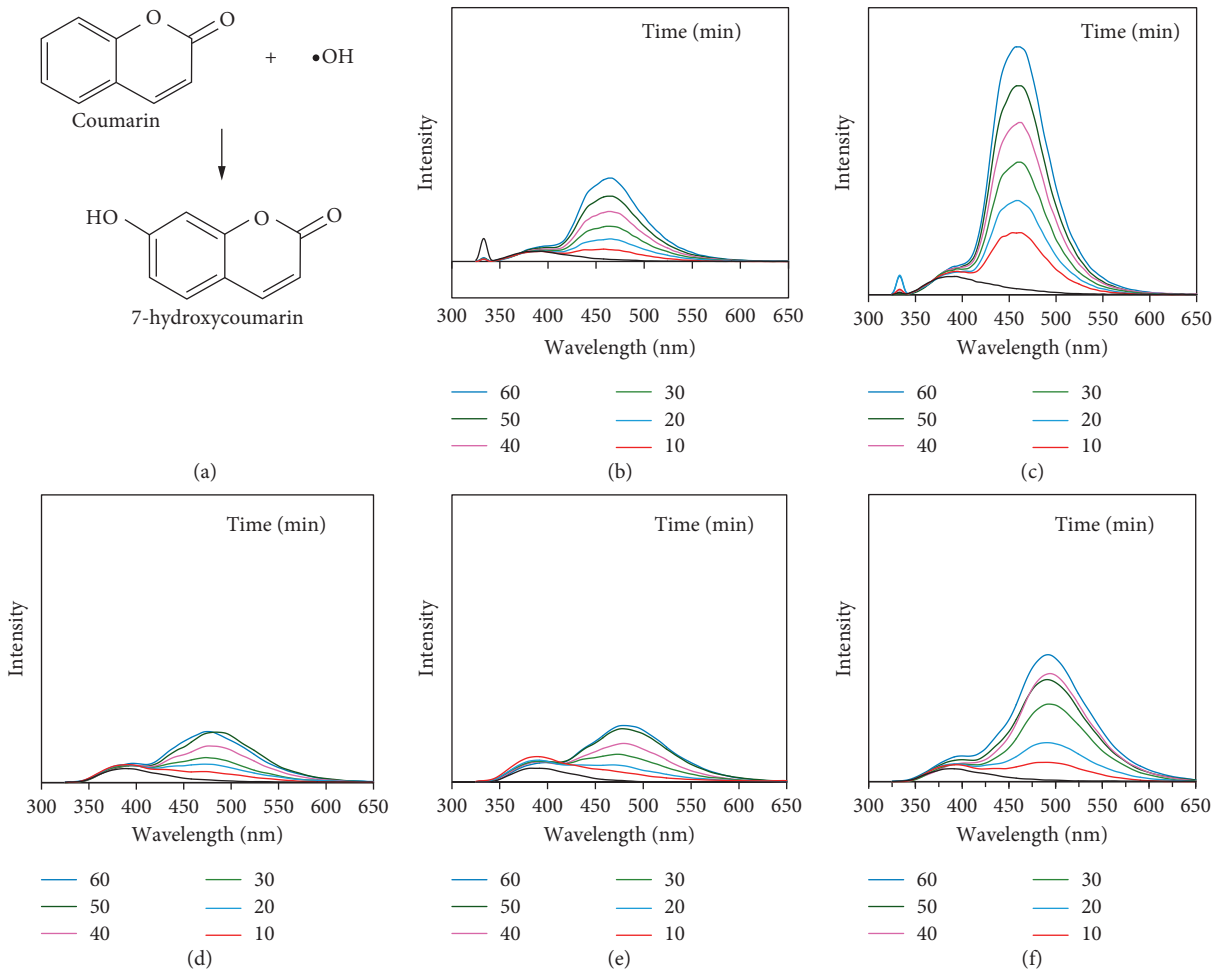

Figure 11: Fluorescence spectra of the 2,4,6-trichlorophenol employed in the detection of $OH^{\bullet}$ generated by photolysis, TiO_2-P25, and M2, M3, and M6 photocatalysts without air bubbling.

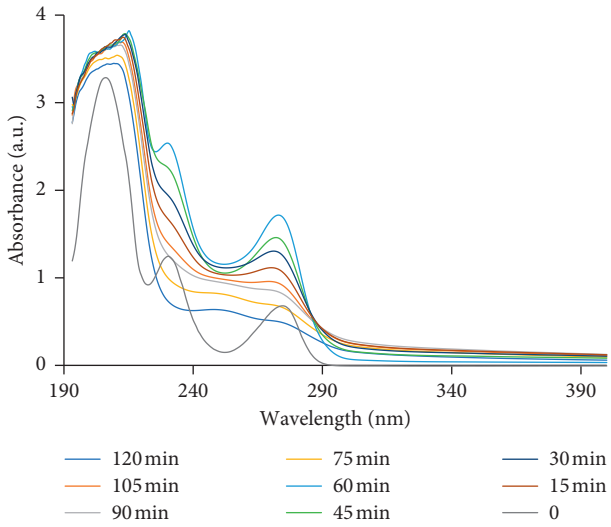

Figure 12: Fluorescence spectra of 2,4,6-trichlorophenol employed in the detection of superoxide radicals generated by the M2 photocatalyst.

Figure 13 shows the pseudo-first-order degradation kinetics and apparent rate constants of the active species $h^+/O_2^{-\bullet}$ of M2 with different scavengers in 2,4,6-trichlorophenol degradation.

To the reaction system of ammonium oxalate, the value of apparent constant for oxalate to $O_2^{-\bullet}$ active species is $51 \times 10^{-4}\,min^{-1}$, with UV-Vis photodegradation of 49%. In the case of the N_2 system, apparent constant with h^+ active species has a value of $26 \times 10^{-4}\,min^{-1}$ and 27% of photodegradation.

Activated hydrotalcites, as photocatalytic materials despite not being considered as semiconductor materials, exhibit photocatalytic capacity when reconstructed by the memory effect after being thermally activated. Their photocatalytic activity is explained by the presence of the electron-hole pairs generated when the hydrotalcites are irradiated with a UV light source (λ = 254 nm), which has energy equal to or greater than the band gap energy of the hydrotalcites, generating electron-hole pairs, in which the electron is delocalized towards the electronic deficiencies of Al^{3+} generating a conduction band and a gap in the valence band. On the contrary, the e^- that are delocalized towards the electrodeficient charge of Al^{3+} react with the dissolved O_2 to form superoxide radicals ($O_2^{-\bullet}$). The superoxides will act as oxidizing photocatalytic species for the degradation of 2,4,6-trichlorophenol [54, 55].

3.5. Kinetic Model Adjustment Study. Table 4 shows the comparison between zero-order kinetic, pseudo-first-order kinetic, and pseudo-second-order kinetic models. The kinetic data were better fitted by the pseudo-first-order model.

In Figure 14, the behavior of the degradation rate of 2,4,6-trichlorophenol is shown as a ratio of the number of molecules degraded per unit of time. It was observed that the photocatalysts M2, M3, and M6 presented greater degradation and better percentage of mineralization. The highest degradation capacity was presented by the M2 catalyst, which reached values of degradation of 2,4,6-trichlorophenol of 100%; it is followed by the M3 catalyst with 96%, M6 with 90%, and so on, decreasing this capacity for the solids M1, M5, and M7 up to values of 77%, where the decrease in the degradation capacity is associated with the physicochemical properties of the materials (low specific area, size crystal, and Mg/Al molar ratio), which are a determining factor in the formation of free radicals [52].

The kinetic study of the photodegradation of 100 ppm of 2,4,6-trichlorophenol with Mg/Al photocatalysts of different ratios showed for all the cases that the data adjust to a pseudo-first-order reaction $\ln(C_0/C) = K_t$, after linearization by least squares with a correlation coefficient of 0.99. The results show a maximum apparent velocity constant for the M1 photocatalysts ($K_{app} = 0.0121\,min^{-1}$) and a minimum for the M7 sample ($K_{app} = 0.0118\,min^{-1}$).

Table 5 shows the data obtained for the calculation of degradation kinetics such as the half-life times, speed constants, and degradation percentage of 2,4,6-trichlorophenol; in this, the photocatalyst M2 500°C is the most active, since it has the shortest half-life of 34.57 min and a degradation percentage of 100%, in a time of 240 min.

3.6. Study of Mineralization. Figure 15 shows the analysis of total organic carbon (TOC), where it can be observed that the degradation of 2,4,6-trichlorophenol reaches up to 80% of mineralization in a time of 240 minutes, for the M2 catalysts; for M3, M4, M7, M1, and M6 mineralization, it is observed between 39 and 85%; in the case of M5, there is no mineralization.

The catalyst that showed a greater efficiency in photocatalytic degradation is M2 500°C with Mg/Al ratio = 2, since it reached 100% degradation of the 100 ppm of 2,4,6-trichlorophenol and mineralized 85%.

3.7. Possible Routes of 2,4,6-Trichlorophenol Degradation Mechanism. Figure 16 shows a diagram with the two main routes or degradation pathways of 2,4,6-trichlorophenol based on the properties of the catalysts and the different types of free radicals involved. As could be demonstrated in the fluorescence test for the detection of generation of superoxide radicals, this is the predominant route involved in the degradation of the contaminant and in a lesser proportional way to the free radicals of hydroxide.

Degradation and mineralization can occur simultaneously, thanks to the presence of superoxide radicals, accompanied by a minor route of hydroxyl radicals, which can be associated with the rapid disappearance of total organic carbon [56, 57].

It has been observed in the UV spectra that the formation of intermediaries of the enones type is not observed, which is a common intermediate in the photodegradation of phenol where parabenzoquinines are formed [58], which would imply that the superoxide radicals are carrying out degradation of the aromatic ring simultaneously with chlorine elimination, although gas chromatography checking is necessary. The superoxide anions generated can be recombined and form singlet oxygen, which could

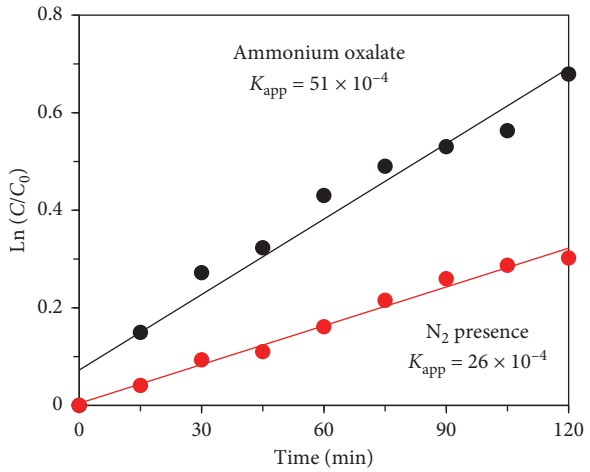

Figure 13: Pseudo-first-order degradation kinetics with different scavengers in 2,4,6-trichlorophenol degradation.

Table 4: Adjusted R square for zero-order kinetic (ZOK), pseudo-first-order (PFO) kinetic, and pseudo-second-order (PSO) kinetic models.

Catalyst	ZOK	PFO	PSO
M1 500°C	0.8398	0.9675	0.9268
M2 500°C	0.9174	0.9860	0.7272
M3 500°C	0.9449	0.9976	0.8544
M4 500°C	0.7824	0.9350	0.9246
M5 500°C	0.9882	0.9690	0.7849
M6 500°C	0.9932	0.9080	0.6787
M7 500°C	0.9602	0.8920	0.7748

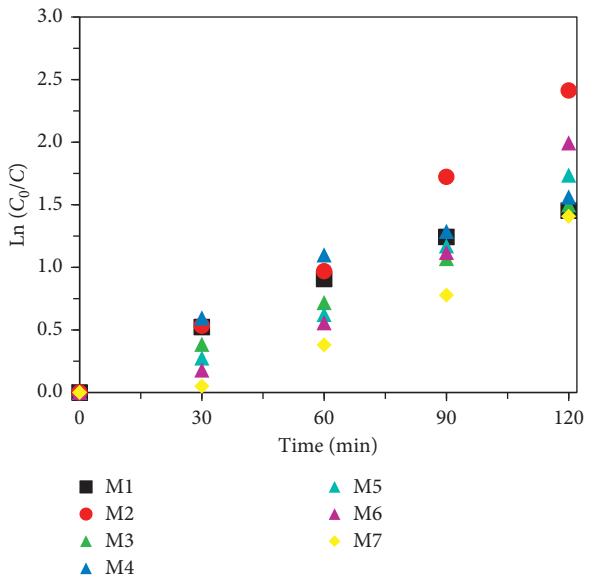

Figure 14: Pseudo-first-order degradation kinetics for 100 ppm of 2,4,6-trichlorophenol with different photocatalysts.

contribute to the degradation of the 2,4,6-trichlorophenol [59, 60].

The rapid and simultaneous degradation/mineralization process that occurs in active hydrotalcites is efficient and

Table 5: Kinetic parameters after 2 hours of reaction time.

Catalyst	K (min^{-1})	$t_{1/2}$ (min)	Photodegradation (%)
M1 500°C	0.0121	57.38	84.0
M2 500°C	0.0200	34.57	100.0
M3 500°C	0.0123	56.49	98.8
M4 500°C	0.0127	67.96	85.5
M5 500°C	0.0146	47.57	98.0
M6 500°C	0.0164	42.21	98.7
M7 500°C	0.0118	58.69	97.8

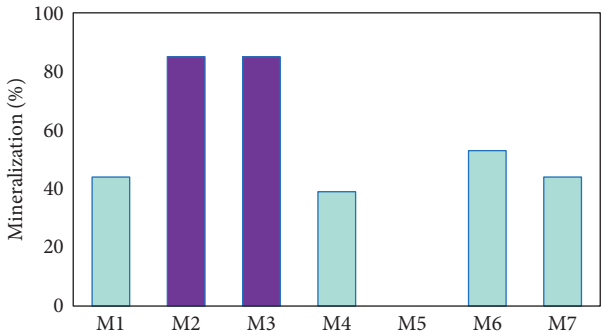

Figure 15: TOC removal during photodegradation of a 2,4,6-trichlorophenol solution.

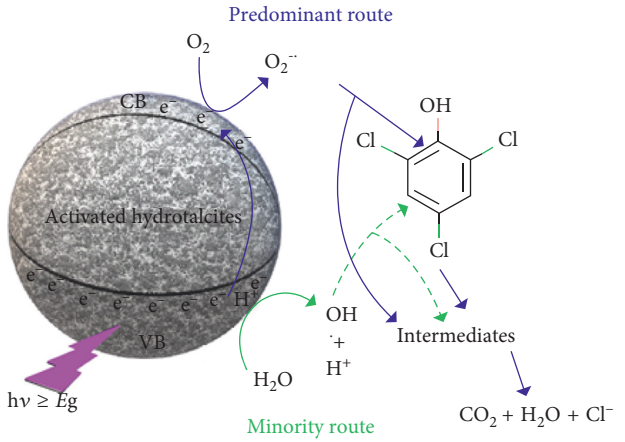

Figure 16: Possible routes for the degradation/mineralization of 2,4,6-trichlorophenol by activated hydrotalcites.

competitive with respect to the different materials that have been used to degrade this stable and persistent pollutant in aqueous systems. The main advantages of activated hydrotalcites are that they are not toxic, are easy to synthesize, and have the ability to regenerate for continued use. As can be seen in Table 6, there is a wide variety of photocatalysts that have been used for the degradation of 2,4,6-trichlorophenol. The main disadvantage of most of these materials is that they need to be doped with transition metals.

3.8. Reconstitution of Hydrotalcites by Memory Effect during Photodegradation. The original 2,4,6-trichlorophenol solution has a pH of 6.0, which is modified by adding

Table 6: Comparison of different photocatalysts used in 2,4,6-trichlorophenol photodegradation.

Photocatalyst	Initial concentration	Experimental condition	Dose (g/L)	Time (min), degradation (%)	Ref.
ZnO-Fe	20 mg/L	65 W, UV-Vis	1	120, 98	[61]
TiO_2@Fe_3O_4-Au	0.1 μM (0.02 mg/L)	105 W, Xe UV-Vis	1	50, 90	[62]
TiO_2-La	10 μM (2 mg/L)	UV-Vis	2	60, 85	[63]
ZnO powder	50 mg/L	6 W, UV lamp	0.75	90, 84	[64]
MMT-Cu H_2O_2	0.1 mM (20 mg/L)	—	0.18	60, 95	[19]
PMS-C	50 mg/L	—	0.75	75, 60	[65]
CdS	200 mg/L	UVC	0.65	180, 88.74	[66]
MCM41-Fe, Co, Ni-H_2O_2	2 mM (400 mg/L)	UV-Vis	2	300, 65	[67]
ZrO_2-polianilyne	5 μM (1 mg/L)	300 W, UV-Vis	0.5	240, 75	[68]
LDH-Cu	1 mg/L	300 W, Xe UV-Vis	0.5	210, 95.1	[69]
Hydrotalcite (this work)	100 mg/L	UV-Vis	1	120, 100	

the hydrotalcite, reaching slightly basic pH during photodegradation. Hydrotalcites at neutral and basic pH are stable, so they do not leach the metals of the sheet. The solid recovered after photodegradation was characterized by XRD and FTIR to identify the effect of the process on the catalyst.

In Figure 17, the X-ray diffraction patterns of the hydrotalcites are shown after the photodegradation reaction, and they are regenerated during the photodegradation process of 2,4,6-trichlorophenol; all the signals of the hydrotalcite are observed, showing a more crystalline reconstruction for solid M1. According to this, it can be verified that the hydrotalcites are restructured to be in the aqueous medium during the photocatalytic degradation of 2,4,6-trichlorophenol due to the memory effect, which is a property characteristic of this type of materials [70].

Figure 18 shows the FTIR spectra of the reconstructed hydrotalcites after photodegradation in which it is observed that the signals in the range of 4000 to 3000 cm^{-1} corresponding to the hydroxyl groups are present in all the spectra in the decreasing order of the catalysts: M1> M2> M3> M4> M6 = M5> M7. A signal is also observed in all samples at 1460 cm^{-1}, corresponding to the vibration frequencies of carbonate groups with different percentages of transmittance in the following order: M1> M2> M4> M6> M3 = M5 = M7.

According to this, it is concluded that the hydrotalcites are restructured to be in the aqueous medium during the photocatalytic degradation of 2,4,6-trichlorophenol due to the memory effect [70]. Thanks to the fact that the catalyst recovers its original structure, it can be reactivated and used in new degradation cycles.

4. Conclusions

The results obtained in studies of the ability of activated hydrotalcites to degrade photocatalytically to 2,4,6-trichlorophenol confirm the potential and suitability of the applicability of these materials. The catalysts present E_g values ranging from 3.45 to 3.56 very close to those of TiO_2. The potential of band gap energy makes the materials with semiconductor properties when irradiated with ultraviolet light capable of generating superoxide and superoxide radicals. The physicochemical properties identified in Mg/Al

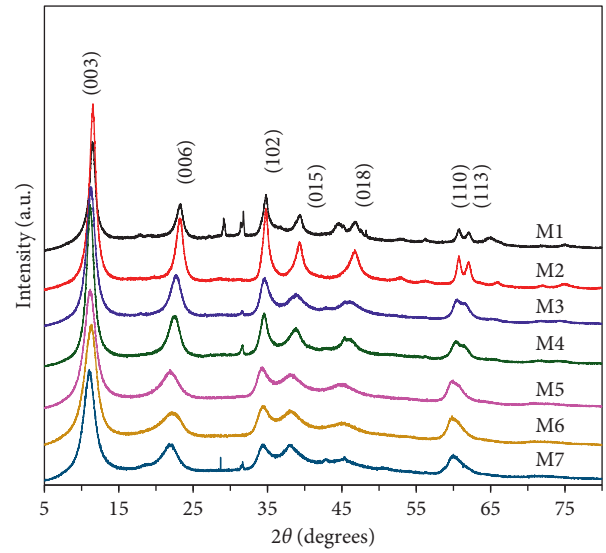

Figure 17: X-ray diffraction of Mg/Al hydrotalcites reconstructed after photodegradation of 2,4,6-trichlorophenol.

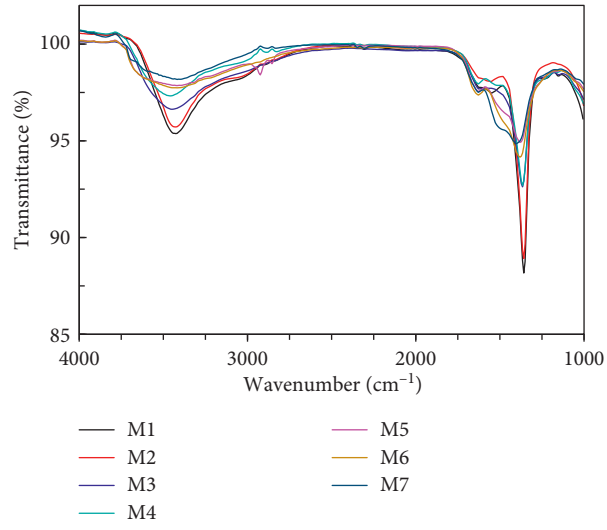

Figure 18: Infrared spectra of the photocatalysts Mg/Al-activated hydrotalcites after photocatalytic degradation of 2,4,6-trichlorophenol.

hydrotalcites, such as their mesoporosity, crystallinity, thermal stability, and their memory effect, make them potential materials to replace TiO_2 and ZnO, as well as the many photocatalytic materials doped with high metals, of higher economic cost and ample toxic potential.

Data Availability

The data used to support the findings of this study are available from the corresponding author upon request.

Conflicts of Interest

The authors declare that they have no conflicts of interest.

Acknowledgments

We would like to especially thank the Directorate for Research and Postgraduate Support (DAIP) at the University of Guanajuato for their support in developing this project. Also, we thank University of Guanajuato-CONACyT National Laboratory SEM-EDX. Additionally, we thank the CONACyT for the graduate scholarship and UAM-I for technical support.

Supplementary Materials

The supplementary file is a graphic summary of the degradation process presented in the article. (*Supplementary Materials*)

References

[1] J. Wilkinson, P. S. Hooda, J. Barker, S. Barton, and J. Swinden, "Occurrence, fate and transformation of emerging contaminants in water: an overarching review of the field," *Environmental Pollution*, vol. 231, pp. 954–970, 2017.

[2] M. S. U. Rehman, N. Rashid, M. Ashfaq, A. Saif, N. Ahmad, and J. I. Han, "Global risk of pharmaceutical contamination from highly populated developing countries," *Chemosphere*, vol. 138, pp. 1045–1055, 2015.

[3] S. Castiglioni, E. Davoli, F. Riva et al., "Mass balance of emerging contaminants in the water cycle of a highly urbanized and industrialized area of Italy," *Water Research*, vol. 131, pp. 287–298, 2018.

[4] J. Coakley, P. Bridgen, M. N. Bates, J. Douwes, and A. Mannetje, "Chlorinated persistent organic pollutants in serum of New Zealand adults, 2011–2013," *Science of The Total Environment*, vol. 615, pp. 624–631, 2018.

[5] J. Chun-Te Lin, K. Sopajaree, T. Jitjanesuwan, and M.-C. Lu, "Application of visible light on copper-doped titanium dioxide catalyzing degradation of chlorophenols," *Separation and Purification Technology*, vol. 191, pp. 233–243, 2018.

[6] M. Honda and K. Kannan, "Biomonitoring of chlorophenols in human urine from several Asian countries, Greece and the United States," *Environmental Pollution*, vol. 232, pp. 487–493, 2018.

[7] V. Geissen, H. Mol, H. Mol et al., "Emerging pollutants in the environment: A challenge for water resource management," *International Soil and Water Conservation Research*, vol. 3, no. 1, pp. 57–65, 2015.

[8] A. Jurado, E. Vàzquez-Suñé, J. Carrera, M. López de Alda, E. Pujades, and D. Barceló, "Emerging organic contaminants in groundwater in Spain: a review of sources, recent occurrence and fate in a European context," *Science of The Total Environment*, vol. 440, pp. 82–94, 2012.

[9] T. Ge, J. Han, Y. Qi et al., "The toxic effects of chlorophenols and associated mechanisms in fish," *Aquatic Toxicology*, vol. 184, pp. 78–93, 2017.

[10] A. O. Olaniran and E. O. Igbinosa, "Chlorophenols and other related derivatives of environmental concern: properties, distribution and microbial degradation processes," *Chemosphere*, vol. 83, no. 10, pp. 1297–1306, 2011.

[11] E. O. Igbinosa, E. E. Odjadjare, V. N. Chigor et al., "Toxicological profile of chlorophenols and their derivatives in the environment: the public health perspective," *Scientific World Journal*, vol. 2013, Article ID 460215, 11 pages, 2013.

[12] A. M. Ruder and J. H. Yiin, "Mortality of US pentachlorophenol production workers through 2005," *Chemosphere*, vol. 83, no. 6, pp. 851–861, 2011.

[13] J. Xiong, C. Hang, J. Gao, Y. Guo, and C. Gu, "A novel biomimetic catalyst templated by montmorillonite clay for degradation of 2,4,6-trichlorophenol," *Chemical Engineering Journal*, vol. 254, pp. 276–282, 2014.

[14] Y. Peng, J. Chen, S. Lu et al., "Chlorophenols in municipal solid waste incineration: a review," *Chemical Engineering Journal*, vol. 292, pp. 398–414, 2016.

[15] Public Health Service, *Agency for Toxic Substances and Disease Registry, Toxicological Profile for Chlorophenols*, U.S. Department of Health and Human Services, Atlanta GA, USA, 1999.

[16] National Toxicology Program, *Department of Health and Human Services, Report on Carcinogens, Fourteenth Edition, 2,4,6-Trichlorophenol, CAS No. 88-06-2*, National Institute of Environmental Health Sciences, Research Triangle Park, NC, USA.

[17] C. Descorme, "Catalytic wastewater treatment: oxidation and reduction processes. Recent studies on chlorophenols," *Catalysis Today*, vol. 297, pp. 324–334, 2017.

[18] J. Á. Pino-Chamorro, T. Ditrói, G. Lente, and I. Fábián, "A detailed kinetic study of the direct photooxidation of 2,4,6-trichlorophenol," *Journal of Photochemistry and Photobiology A: Chemistry*, vol. 330, pp. 71–78, 2016.

[19] F. Ghanbari, M. Moradi, and F. Gohari, "Degradation of 2,4,6-trichlorophenol in aqueous solutions using peroxymonosulfate/activated carbon/UV process via sulfate and hydroxyl radicals," *Journal of Water Process Engineering*, vol. 9, pp. 22–28, 2016.

[20] N. Inchaurrondo, C. P. Ramos, G. Zerjav, J. Font, A. Pintar, and P. Haure, "Modified diatomites for Fenton-like oxidation of phenol," *Microporous and Mesoporous Materials*, vol. 239, pp. 396–408, 2017.

[21] L. Martínkova, M. Kotik, E. Markova, and L. Homolka, "Biodegradation of phenolic compounds by *Basidiomycota* and its phenol oxidases: a review," *Chemosphere*, vol. 149, pp. 373–382, 2016.

[22] H. Zhang, W. Xu, Z. Fan, X. Liu, Z. Wua, and M. Zhou, "Simultaneous removal of phenol and dichromate from aqueous solution through a phenol-Cr(VI) coupled redox fuel cell reactor," *Separation and Purification Technology*, vol. 172, pp. 152–157, 2017.

[23] N. Singh and C. Balomajumder, "Batch growth kinetic studies for elimination of phenol and cyanide using mixed microbial culture," *Journal of Water Process Engineering*, vol. 11, pp. 130–137, 2016.

[24] A. Mukimin, N. Zen, A. Purwanto, K. A. Wicaksono, H. Vistanty, and A. S. Alfauzi, "Application of a full-scale electrocatalytic reactor as real batik printing wastewater treatment by indirect oxidation process," *Journal of Environmental Chemical Engineering*, vol. 5, no. 5, pp. 5222–5232, 2017.

[25] A. J. Barik and P. R. Gogate, "Hybrid treatment strategies for 2,4,6-trichlorophenol degradation based on combination of hydrodynamic cavitation and AOPs," *Ultrasonics Sonochemistry*, vol. 40, pp. 383–394, 2018.

[26] C. Byrne, G. Subramanian, and S. C. Pilliai, *Journal of Environmental Chemical Engineering*, vol. 6, no. 3, pp. 3531–3555, 2017.

[27] C. B. Onga, L. Y. Ngb, and A. W. Mohammada, "A review of ZnO nanoparticles as solar photocatalysts: synthesis, mechanisms and applications," *Renewable and Sustainable Energy Reviews*, vol. 81, pp. 536–551, 2018.

[28] E. Bailón-García, A. Elmouwahidi, F. Carrasco-Marín, A. F. Pérez-Cadenas, and F. J. Maldonado-Hódar, "Development of Carbon-ZrO2 composites with high performance as visible-light photocatalysts," *Applied Catalysis B: Environmental*, vol. 217, pp. 540–550, 2017.

[29] S. G. Kumar and K. S. R. Koteswara, "Tungsten-based nanomaterials (WO 3 & Bi 2 WO 6): Modifications related to charge carrier transfer mechanisms and photocatalytic applications," *Applied Surface Science*, vol. 355, pp. 939–958, 2015.

[30] H. Song, R. Wu, J. Yang, J. Dong, and G. Ji, "Fabrication of CeO_2 nanoparticles decorated three-dimensional flower-like BiOI composites to build p-n heterojunction with highly enhanced visible-light photocatalytic performance," *Journal of Colloid and Interface Science*, vol. 512, pp. 325–334, 2018.

[31] S. Anandan, Y. Ikuma, and V. Murugesan, "Highly active rare-earth-metal La-doped photocatalysts: fabrication, characterization, and their photocatalytic activity," *International Journal of Photoenergy*, vol. 2012, Article ID 921412, 10 pages, 2012.

[32] S. J. Ki, K. Jeon, Y. Park, S. Jeong, H. Leed, and S. Jung, "Improving removal of 4-chlorophenol using a TiO_2 photocatalytic system with microwave and ultraviolet radiation," *Catalysis Today*, vol. 293–294, pp. 15–22, 2017.

[33] M. Antonopoulou, P. Karagianni, A. Giannakas et al., "Photocatalytic degradation of phenol by char/N-TiO_2 and char/N-F-TiO_2 composite photocatalysts," *Catalysis Today*, vol. 280, pp. 114–121, 2017.

[34] J. Wang, B. Wei, L. Xu, H. Gao, W. Sun a, and J. Che, "Multilayered MoS_2 coated TiO_2 hollow spheres for efficient photodegradation of phenol under visible light irradiation," *Materials Letters*, vol. 179, pp. 42–46, 2016.

[35] M. F. Almeida, C. R. Bellato, A. H. Mounteer, S. O. Ferreirac, J. L. Milagres, and L. D. Lima, "Enhanced photocatalytic activity of TiO_2 -impregnated with MgZnAl mixed oxides obtained from layered double hydroxides for phenol degradation," *Applied Surface Science*, vol. 357, pp. 1765–1775, 2015.

[36] K. Abderrazek, F. Srasra Najoua, and E. Srasra, "Synthesis and characterization of [Zn–Al] LDH: Study of the effect of calcination on the photocatalytic activity," *Applied Clay Science*, vol. 119, pp. 229–235, 2016.

[37] X. Liang, X. Yang, G. Gao et al., "Performance and mechanism of CuO/CuZnAl hydrotalcites-ZnO for photocatalytic selective oxidation of gaseous methanol to methyl formate at ambient temperature," *Journal of Catalysis*, vol. 339, pp. 68–76, 2016.

[38] J. Zhu, Z. Zhu, H. Zhang et al., "Enhanced photocatalytic activity of Ce-doped Zn-Al multi-metal oxide composites derived from layered double hydroxide precursors," *Journal of Colloid and Interface Science*, vol. 481, pp. 144–157, 2016.

[39] J. Yang, H. Chen, J. Gao et al., "Synthesis of Fe_3O_4/g-C_3N_4 nanocomposites and their application in the photodegradation of 2,4,6-trichlorophenol under visible light," *Materials Letters*, vol. 164, pp. 183–189, 2016.

[40] M. Mureseanu, T. Radu, R. Andrei, M. Darie, and G. Carja, "Green synthesis of g-C_3N_4 /CuONP/LDH composites and derived g-C_3N_4 /MMO and their photocatalytic performance for phenol reduction from aqueous solutions," *Applied Clay Science*, vol. 141, pp. 1–12, 2017.

[41] Z. Timár, G. Varga, S. Muráth et al., "Synthesis, characterization and photocatalytic activity of crystalline Mn(II) Cr(III)-layered double hydroxide," *Catalysis Today*, vol. 284, pp. 195–201, 2017.

[42] C. Dai, A. Zhang, L. Luo et al., "Hollow zeolite-encapsulated Fe-Cu bimetallic catalysts for phenol degradation," *Catalysis Today*, vol. 297, pp. 335–343, 2017.

[43] S. Kima, P. Durand, E. André, and C. Carteret, "Enhanced photocatalytic ability of Cu, Co doped ZnAl based mixed metal oxides derived from layered double hydroxides," *Colloids and Surfaces A: Physicochemical and Engineering Aspects*, vol. 524, pp. 43–52, 2017.

[44] M. Hadnadjev-Kostic, T. Vulic, R. Marinkovic-Neducin et al., "Photo-induced properties of photocatalysts: a study on the modified structural, optical and textural properties of TiO_2–ZnAl layered double hydroxide based materials," *Journal of Cleaner Production*, vol. 164, pp. 1–18, 2017.

[45] A. Elhalil, R. Elmoubarki, A. Machrouhi et al., "Photocatalytic degradation of caffeine by ZnO-$ZnAl_2O_4$ nanoparticles derived from LDH structure," *Journal of Environmental Chemical Engineering*, vol. 5, no. 4, pp. 3719–3726, 2017.

[46] K. Choi, S. Park, B. J. Park, and J. Jung, "Recyclable Ag-coated Fe_3O_4 @TiO_2 for efficient photocatalytic oxidation of chlorophenol," *Surface and Coatings Technology*, vol. 320, pp. 240–245, 2017.

[47] F. Wypych and K. G. Satyanarayana, *Clay surfaces–Fundamentals and Applications: Interface Science and Techology*, Elsevier Press, Vol. 1, Elsevier Press, Cambridge, MA, USA, 2004.

[48] D. S. Tong, C. H. Zhou, M. Y. Li et al., "Structure and catalytic properties of Sn-containing layered double hydroxides synthesized in the presence of dodecylsulfate and dodecylamine," *Applied Clay Science*, vol. 48, no. 4, pp. 569–574, 2010.

[49] A. A. A. Ahmed, Z. A. Talib, and M. Z. Hussein, "Thermal, optical and dielectric properties of Zn–Al layered double hydroxide," *Applied Clay Science*, vol. 56, pp. 68–76, 2012.

[50] B. Pourabbas and B. Jamshidi, "Preparation of MoS_2 nanoparticles by a modified hydrothermal method and the photocatalytic activity of MoS_2/TiO_2 hybrids in photo-oxidation of phenol," *Chemical Engineering Journal*, vol. 138, pp. 55–62, 2008.

[51] A. Yi, Y. Feng, Z. Du, and H. Li, *International Journal of Electrochemical Science*, vol. 10, pp. 1459–1468, 2015.

[52] M. Jabłońska, L. Chmielarz, A. Węgrzyn et al., "Hydrotalcite derived (Cu, Mn)–Mg–Al metal oxide systems doped with palladium as catalysts for low-temperature methanol incineration," *Applied Clay Science*, vol. 114, pp. 273–282, 2015.

[53] K. Ishibashi, A. Fujishima, T. Watanabe, and K. Hashimoto, "Detection of active oxidative species in TiO2 photocatalysis using the fluorescence technique," *Electrochemistry Communications*, vol. 2, no. 3, pp. 207–210, 2000.

[54] L. Mohapatra and K. M. Parida, "Zn–Cr layered double hydroxide: visible light responsive photocatalyst for photocatalytic degradation of organic pollutants," *Separation and Purification Technology*, vol. 91, pp. 73–80, 2012.

[55] X. Wang, S. Wang, and W. Hu, "Synthesis and photocatalytic activity of SiO_2/g-C_3N_4 composite photocatalyst," *Materials Letters*, vol. 115, pp. 53–56, 2014.

[56] M. Aslam, M. T. Qamar, M. Tahir Soomro et al., "The effect of sunlight induced surface defects on the photocatalytic activity of nanosized CeO_2 for the degradation of phenol and its derivatives," *Applied Catalysis B: Environmental*, vol. 180, pp. 391–402, 2016.

[57] M. Aslam, M. T. Qamar, S. Ali et al., "Evaluation of SnO_2 for sunlight photocatalytic decontamination of water," *Journal of Environmental Management*, vol. 217, pp. 805–814, 2018.

[58] F. Nawaz, Y. Xie, J. Xiao, H. Cao, Y. Li, and D. Zang, "Insights into the mechanism of phenolic mixture degradation by catalytic ozonation with a mesoporous Fe_3O_4/MnO_2 composite," *RSC Advances*, vol. 6, no. 35, pp. 29674–29684, 2016.

[59] N. Jaafarzadeh, G. Barzegar, and F. Ghanbari, "Photo assisted electro-peroxone to degrade 2,4-D herbicide: The effects of supporting electrolytes and determining mechanism," *Process Safety and Environmental Protection*, vol. 111, pp. 520–528, 2017.

[60] M. Ahmadi and F. Ghanbari, "Combination of UVC-LEDs and ultrasound for peroxymonosulfate activation to degrade synthetic dye: influence of promotional and inhibitory agents and application for real wastewater," *Environmental Science and Pollution Research*, vol. 25, no. 6, pp. 6003–6014, 2018.

[61] A. V. Lav and YS. Malgue, "Synthesis, characterization and visible light photocatalytic activity of carbon and iron modified ZnO," *Journal of King Saud University-Science*, vol. 30, no. 1, pp. 65–74, 2018.

[62] C. Kyong-Hoon, P. So-Yeong, B. P. Joo, and J. Jin-Seung, "Recyclable Ag-coated Fe_3O_4 @TiO_2 for efficient photocatalytic oxidation of chlorophenol," *Surface and Coatings Technology*, vol. 320, pp. 240–245, 2017.

[63] H. Peng, J. Cui, H. Zhan, and X. Zhang, "Improved photodegradation and detoxification of 2,4,6-trichlorophenol by lanthanum doped magnetic TiO_2," *Chemical Engineering Journal*, vol. 264, pp. 316–321, 2015.

[64] U. I. Gaya, A. H. Abdullah, M. Z. Hussein, and Z. Zainal, "Photocatalytic removal of 2,4,6-trichlorophenol from water exploiting commercial ZnO powder," *Desalination*, vol. 263, no. 1–3, pp. 176–182, 2010.

[65] F. Khodadadeh, P. A. Azar, M. S. Tehrani, and N. Assi, "Photo catalytic property of ZnO and Mn-ZnO nanoparticles in removal of Cibacet Turquoise blue G from aquatic solution," *International Journal of Nano Dimension*, vol. 7, pp. 263–269, 2016.

[66] S. Chaliha and K. G. BhattaChariya, "Wet oxidative method for removal of 2,4,6-trichlorophenol in water using Fe(III), Co(II), Ni(II) supported MCM41 catalysts," *Journal of Hazardous Materials*, vol. 150, no. 3, pp. 728–736, 2018.

[67] M. V. Carevic, N. D. Abazovic, M. N. Mitric et al., "Properties of Zirconia/Polyaniline hybrid nanocomposites and their application as photocatalysts for degradation of model pollutants," *Materials Chemistry and Physics*, vol. 205, pp. 130–137, 2018.

[68] H. Zangeneh, A. A. Zinatizadeh, M. Feyzi, S. Zinadini, and D. W. Bahnemann, "Photomineralization of recalcitrant wastewaters by a novel magnetically recyclable boron doped-TiO_2-SiO_2 cobalt ferrite nanocomposite as a visible-driven heterogeneous photocatalyst," *Journal of Environmental Chemical Engineering*, vol. 6, no. 5, pp. 6370–6381, 2018.

[69] S. Xia, X. Zhang, X. Zhou, and Y. Meng, "The influence of different Cu species onto multi-copper-contained hybrid materials' photocatalytic property and mechanism of chlorophenol degradation," *Applied Catalysis B: Environmental*, vol. 214, pp. 78–88, 2017.

[70] K. L. Erickson, T. E. Bostrom, and R. L. Frost, "A study of structural memory effects in synthetic hydrotalcites using environmental SEM," *Materials Letters*, vol. 59, no. 2-3, pp. 226–229, 2004.

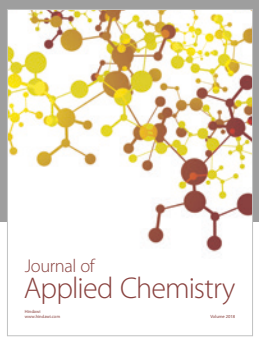

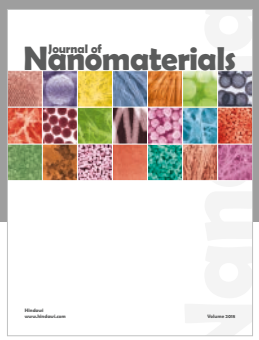

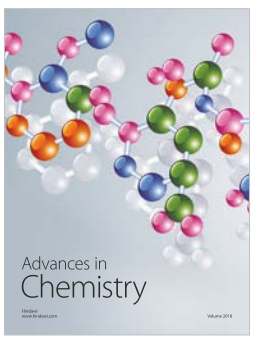
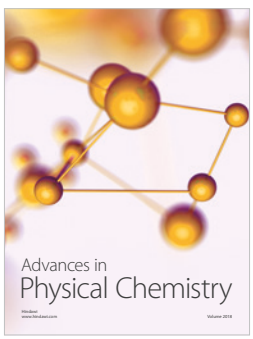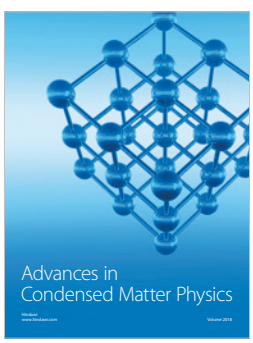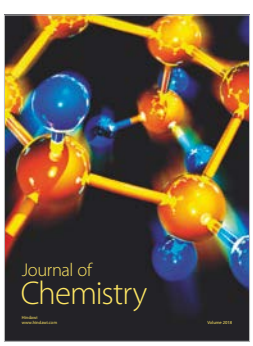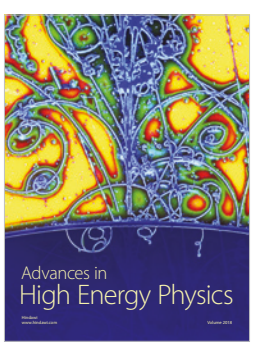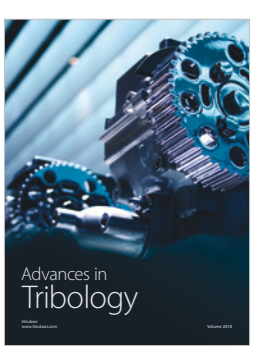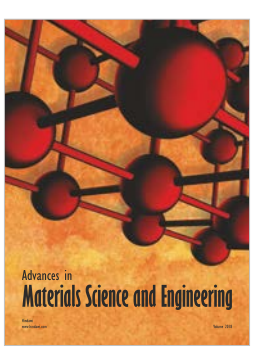
Hindawi
Submit your manuscripts at
www.hindawi.com